# High-Temperature (550–700°C) Chlorosilane Interactions with Iron

**Josh Aller,[a,*,z] Ryan Mason,[b] Kelly Walls,[a] Greg Tatar,[b] Nathan Jacobson,[c] and Paul Gannon[b,**]**

[a]*Mechanical and Industrial Engineering, Montana State University, Bozeman, Montana 59717, USA*
[b]*Chemical and Biological Engineering, Montana State University, Bozeman, Montana 59717, USA*
[c]*NASA Glenn Research Center, Cleveland, Ohio 44135, USA*

Chlorosilane species are commonly used at high temperatures in the manufacture and refinement of ultra-high purity silicon and silicon materials. The chlorosilane species are often highly corrosive in these processes, necessitating the use of expensive, corrosion resistant alloys for the construction of reactors, pipes, and vessels required to handle and produce them. In this study, iron, the primary alloying component of low cost metals, was exposed to a silicon tetrachloride-hydrogen vapor stream at industrially-relevant times (0–100 hours), temperatures (550–700°C), and vapor stream compositions. Post exposure analyses including FE-SEM, EDS, XRD, and gravimetric analysis revealed formation and growth of stratified iron silicide surface layers, which vary as a function of time and temperature. The most common stratification after exposure was a thin FeSi layer on the surface followed by a thick stoichiometric $Fe_3Si$ layer, a silicon activity gradient in an iron lattice, and finally, unreacted iron. Speculated mechanisms to explain these observations were supported by thermodynamic equilibrium simulations of experimental conditions. This study furthers the understanding of metals in chlorosilane environments, which is critically important for manufacturing the high purity silicon required for silicon-based electronic and photovoltaic devices.
 [DOI: 10.1149/2.0681610jes] 

Manuscript submitted July 1, 2016; revised manuscript received August 8, 2016. Published August 18, 2016. This article is a version of Paper 1217 from the Honolulu, Hawaii, Meeting of the Society, October 2–7, 2016.

Chlorosilane species are abundant in the manufacture of ultra-high purity silicon and silicon compounds required for electronic devices and solar panels.[1–4] In general, chlorosilanes are species that contain silicon, chlorine, and/or hydrogen such as silicon tetrachloride ($SiCl_4$, STC), trichlorosilane ($HSiCl_3$, TCS), dichlorosilane ($H_2SiCl_2$, DCS), and silane ($SiH_4$). In industry, they are generally combined with hydrogen ($H_2$) as a carrier gas and hydrogen chloride (HCl) as a by-product of processing.[1–4] These chlorosilanes are used at various steps in the semiconductor and solar panel production processes including silicon refining, silicon deposition, and production of silicides. Each of these processes includes steps at high temperatures, making it necessary to understand how chlorosilanes interact with the pipes, vessels, and reactors tasked with containing them. Without question, the most prevalent structural metal in the world is iron. This is also true in the silicon processing industries where many vessels and pipes are made from various types of steels and stainless steels. While it is important to understand how each specific type of steel interacts with chlorosilanes, it is also essential to study the behavior of pure iron in chlorosilane environments. A thorough understanding of how iron interacts with chlorosilanes will enable the identification of corrosion mechanisms. This will allow metallurgists and engineers to design inexpensive alloys that resist chlorosilane attack.

The presence of both silicon and chlorine in chlorosilanes creates a unique corrosion environment due to iron's ability to form both iron silicides and iron chlorides. Iron chloride formation has been studied extensively due to the presence of chlorides in many oxidizing environments.[5–7] Chloride compounds can form from the interaction of iron with hydrogen chloride, chlorine, or many other chlorine containing species. Iron chlorides have a relatively high vapor pressure,[5,8] causing them to reactively evaporate at high temperatures. This type of interaction causes uncontrollable mass loss corrosion and is problematic for industry.

Iron silicides have also been studied and their formation generally tends to be less problematic from a corrosion standpoint.[6,9] There are several ways to form iron silicides including gas-solid interactions and solid-solid interactions. In either case, the result is a series of stratified surface layers that develop in the iron substrate with different stoichiometry based on the gradient of silicon activity. A few solid-gas interactions of note came from Rebhan et al. when they studied the chemical vapor deposition (CVD) of silicon on to iron.[10,11] The goal of their research was to characterize the CVD process using silane as a feed gas to deposit silicon and then oxidize it to form silica ($SiO_2$). The silica would then act as an adhesion layer between the iron substrate and a polymer coating. They found that they formed silicides, primarily $Fe_3Si$, rather than depositing silicon during their experiments at less than 600°C. During experiments at 800°C and higher silicon was deposited onto the iron substrate and it subsequently diffused in to the iron. They then oxidized this deposited silicon to form their silica adhesion layer. Klam et al. also published an interesting solid-gas interaction study that looked at the influence of silicon source.[12] With a silane source the silicon tends to go into solution in the iron prior to preferentially forming $Fe_3Si$ at the grain boundaries. With a STC silicon source, they found primarily $Fe_3Si$ after exposure with some amount of open porosity. This open porosity was not present in the experiments with silane, and it is suspected that they form from the reaction of either iron or iron silicide to form volatile iron chloride. This paper was also focused on CVD properties, so the exposure temperatures were quite high (750–1100°C).

Baldwin and Ivey studied the solid-solid interaction of silicon and iron by annealing diffusion couples in a vacuum at 700–800°C and times up to several months.[13,14] Their first experiment involved a Fe-Si couple, and they found that there are 3 very distinct iron silicide compounds that form; $Fe_3Si$, FeSi, and $FeSi_2$ developing in that order. There is very little concentration variation within the layers, contrary to the Fe-Si phase diagram.[15] Their next experiment involved a $Fe_3Si$-Fe diffusion couple. In this couple, they were able to form a slow growing non-stoichiometric $Fe_{3+x}Si_{1-x}$ layer as predicted by the phase diagram. Their conclusions from this work were that stoichiometric $Fe_3Si$ grows preferentially and more quickly than non-stoichiometric $Fe_{3+x}Si_{1-x}$. This result is valuable because it lays the framework for understanding the iron silicide formation and growth processes.

There have been some previous studies investigating the corrosion behavior of iron based metals in STC environments. Acker did a significant amount of work characterizing the behavior of metals in chlorosilane environments both as a way to synthesize metal silicides and catalyze the conversion of STC to TCS for polysilicon production.[16–18] Mui also studied the corrosion behavior of many structural high temperature metals in a chlorosilane environment simulated by a packed

*Electrochemical Society Student Member.
**Electrochemical Society Member.
[z]E-mail: josh.aller@yahoo.com

bed reactor.[9] However, his work was largely application based and did not focus on the underlying mechanisms of chlorosilane corrosion. Additionally, the authors have done some work in the field of chlorosilane corrosion of 316L stainless steel.[19–21] Again, this work was largely studying the implications of using 316L in chlorosilane environments rather than investigating the specific mechanisms of corrosion. To the best knowledge of the authors, there are no published studies detailing the corrosion mechanisms of iron in chlorosilane environments representative of industrial processes. The objective of this paper is to study the interactions between iron, STC, and hydrogen at times and temperatures relevant to industry; providing further understanding of the use of low cost iron based alloys in chlorosilane environments.

## Experimental

The authors have described the methods for exposing samples to a STC environment previously,[19] but for clarity, they will briefly be described here. The corrosion testing system (diagram shown previously[19]) used for these experiments created a hydrogen/STC environment by bubbling an adjustable amount of hydrogen gas into the bottom of a bottle of liquid STC. As the hydrogen bubbles rose through the STC, they become fully saturated with STC making the head space a consistent mixture of hydrogen gas and STC vapor. This mixture then flowed out of the bottle through a needle in the cap where it was combined with make-up hydrogen and flowed in to the tube furnace and across the samples. All lines between the STC bottle and the furnace were heat taped to ensure the STC did not condense out of the line. The mass of the STC bottle was measured before and after exposure to calculate the total mass of STC added to the system. Typical mole fractions of hydrogen and STC delivered to the tube furnace were 0.74 and 0.26 respectively. The total flow rate of approximately 80 SCCM combined with a tube diameter of 26.8 mm led to a gas velocity of approximately 14 cm/min. System pressure was not measured explicitly, however there is a release mechanism in the scrubbing system set at approximately 70 kPa. Flat samples were used with a tubular crucible allowing for gas flow on all sides. The samples were exposed to temperatures ranging from 550–700°C for 8–100 hours continuously. The entire system was purged with nitrogen before and during the oven heat-up period, and during the oven cool down period to minimize iron oxidation.

The iron samples used in these tests were 99.6% pure with impurities of 0.025 weight % carbon, 0.03 weight % chromium, 0.04 weight % copper, 0.18 weight % manganese, 0.05 weight % nickel, 0.012 weight % phosphorous, 0.025 weight % sulfur, and 0.05 weight % silicon. They had a 1200 grit finish, were cut to approximately 12 mm × 12 mm × 1.5 mm, deburred, and rinsed with isopropanol and water prior to exposure. All exposures were done in triplicate for statistical relevance. Figures include a 95% confidence interval on the mean of the triplicate samples.

Gravimetric, surface, and cross sectional analysis were performed before and after chlorosilane exposure. Gravimetric analysis utilized a Sartorius microbalance with 2 microgram precision. Mass change was normalized by sample surface area as is standard in this type of analysis. Two types of data transformations were used in this gravimetric analysis. For temperature dependent results, the natural log of specific mass change after a constant time interval was plotted against 1000/(absolute temperature) to show changes in corrosion mechanism. For a single mechanism, this plot will result in a line with the slope of the line being representative of the activation energy for that mechanism. Deviations from this line or changes in slope represent a change in activation energy, and therefore, a change in corrosion mechanism. The other gravimetric data transformation performed in this paper was on time dependent data to check for fit with parabolic kinetics. For this plot, specific mass changes were plotted against the square root of time. If the data are purely parabolic, this plot will result in a straight line that goes through zero with the slope of that line equal to the square root of the parabolic rate constant. Deviations from this line represent non parabolic kinetics.

Surface analysis made use of a Zeiss Supra 55VP field emission scanning electron microscope (FEM) equipped with an energy dispersive X-ray spectroscopy (EDS) system capable of spot, line, and area scans. Atomic concentrations were extracted from the EDS spectra without the use of standards, so results should be interpreted qualitatively rather than quantitatively. X-Ray Diffraction (XRD) was employed using a SCINTAG X1 diffraction system and Jade software for pattern analysis. Cross sections were prepared using Allied High Tech cross sectioning and polishing equipment. Polished cross sections allow for topographic and spectral analysis as a function of depth; displaying any layers that exist. XRD confirms the presence of any crystalline compounds that may be present and cross sectional FEM/EDS suggests where these compounds are located relative to one another, making the combination of the two techniques quite powerful.

Predominance diagrams were produced using FactSage thermodynamic calculation package and FactPS database.[22] The predominance diagrams for this work display the activity of HCl on the horizontal axis and the activity of silicon on the vertical axis with iron as the base metal. The regions inside the diagram represent the stable condensed phases based on the conditions. These types of diagrams are useful to predict stratification of various layers based on the conditions. Temperature-composition phase diagrams were also a part of the theoretical analysis of these experiments. Phase diagrams predict stable species or mixtures of species based on the composition and temperature. In this application, the iron-silicon phase diagram was used to predict what phases were present based on silicon content and the predominance diagram was used to predict location of various phases. While phase diagrams can be constructed with FactSage, the resulting iron-silicon phase diagram does not match the generally accepted diagram first constructed by Kubaschewski[23] and then confirmed by Ohnuma et al.[15] Because of this discrepancy, the diagram published by Ohnuma et al. was used for analysis and the FactSage diagram was not.

## Results

***Temperature dependence of corrosion.—***The first series of exposures was designed to explore the temperature dependence of iron behavior in chlorosilane environments. For these tests, iron was exposed to an input mole fraction of 0.74 $H_2$ and 0.26 STC for 100 hours at 550–700°C. The specific mass change from this series of exposures is displayed in Figure 1a, and the FEM micrographs are displayed in Figure 2. It appears from these figures that the three high temperature exposures resulted in very similar topography, with the higher temperature only making the nodules larger. Additionally, the corrosion scales formed at high temperature all had consistent surface compositions in line with stoichiometric FeSi as measured by EDS. The exposure at 550°C resulted in a much different topography which included much finer nodules and large, high aspect ratio flakes. Additionally, the EDS spectra revealed surface regions consistent in composition with Fe and $Fe_3Si$. The transformed gravimetric data shown in Figure 1b shows some differences in the 550°C exposure compared to the higher temperature exposures. The three high temperature data points form a straight line, while the 550°C data does not fall on this line. The differences between the 550°C data and the 600–700°C data may indicate that they are experiencing different corrosion mechanisms or that they are at different stages in the corrosion process.

This is further supported by the XRD data displayed in Figure 3. In this figure, the XRD patterns from 40–50 two theta are displayed. This range focuses on major Fe, FeSi, and $Fe_3Si$ peaks.[24–26] For the 700, 650, and 600°C exposures, there was a significant amount of FeSi and $Fe_3Si$ detected. The higher temperatures made the FeSi peak more pronounced, perhaps indicating that the higher temperature formed a thicker FeSi layer on top of a $Fe_3Si$ layer. There is also a very small Fe peak present in these patterns, indicating that there is some unreacted Fe remaining in the analyzed area after exposure. In the sample after 650°C exposure, there is an unidentified peak at approximately 45.8

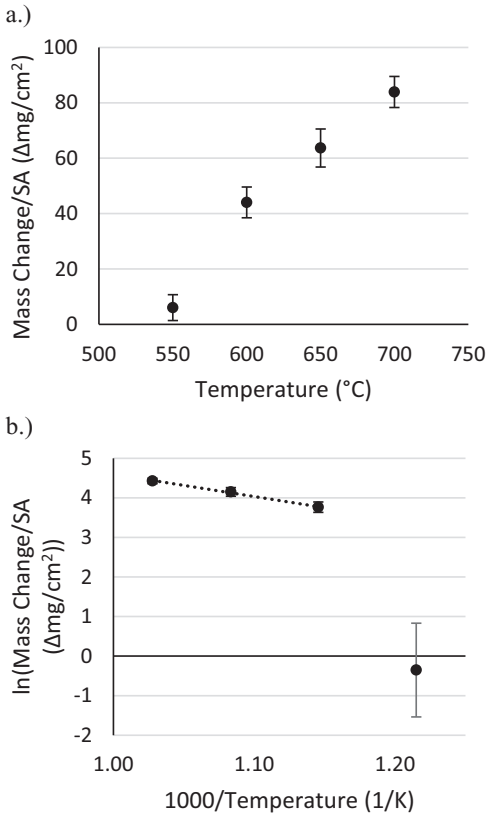


**Figure 1.** The a) specific mass change data and b) transformed gravimetric data for the temperature dependent study. The transformed data plots the natural log of mass change vs the inverse of absolute temperature. This transformation helps identify changes in corrosion mechanism. A linear trend line for the three higher temperature data points is displayed in b. The error bars represent a 95% confidence interval on the mean.

two theta. However, this peak and its associated species appeared to be an anomaly as it was not seen in other exposures. For the sample exposed to chlorosilanes at 550°C, there are some drastic differences compared to the higher temperature runs. The 550°C samples had a much larger Fe peak, indicating a thinner corrosion layer. The iron peak was located at a higher 2 theta value than as received iron, likely

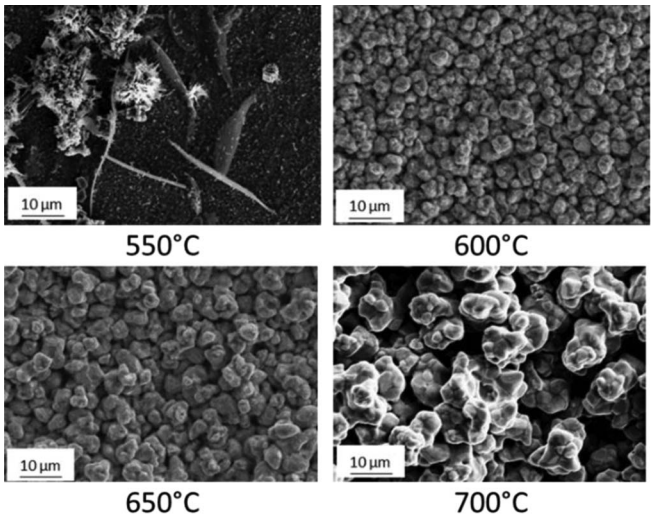


**Figure 2.** The plan view FEM micrographs for the temperature dependent study. These samples were exposed to a STC/$H_2$ environment for 100 hours at 550, 600, 650, and 700°C.

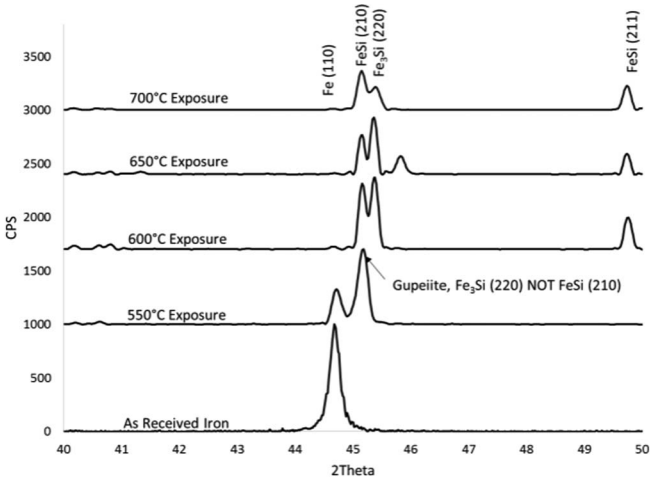


**Figure 3.** The XRD patterns for iron samples after exposure to chlorosilane environments at 550, 600, 650, and 700°C for 100 hours.

due to lattice contraction from the substitutional solution of silicon. This phenomena has been previously reported in the literature for ferritic iron-silicon alloys.[27–30] The amount of contraction due to the addition of silicon varies between studies, but the literature is in agreement with the overall trend. The measured lattice contraction of 0.003 Angstroms is in the range of expected values for a saturated solution of silicon. Also in the 550°C study, there was a $Fe_3Si$ (Gupeiite)[31] structure that formed rather than the $Fe_3Si$ found at the higher temperatures. The Gupeiite peak was differentiated from the FeSi (210) peak using the presence of the FeSi (211) peak. The corroboration of the transformed gravimetric data and the XRD patterns indicate that the corrosion of iron in chlorosilanes at 550°C is mechanistically different than corrosion in a similar environment at 600–700°C.

Cross sectional images and EDS line scans were also performed in this study. Figure 4 shows the cross section of a sample after 100 hours

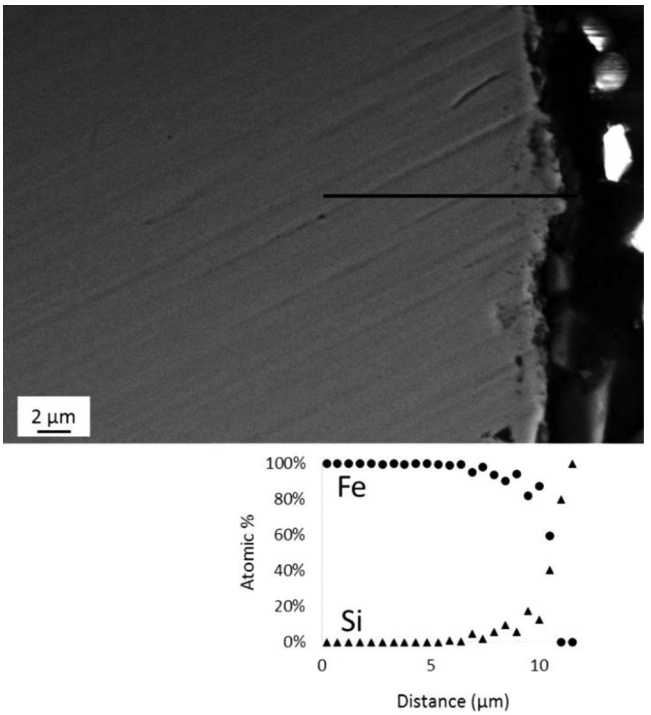


**Figure 4.** High magnification cross sectional image of a sample after exposure to a chlorosilane environment for 100 hours at 550°C.

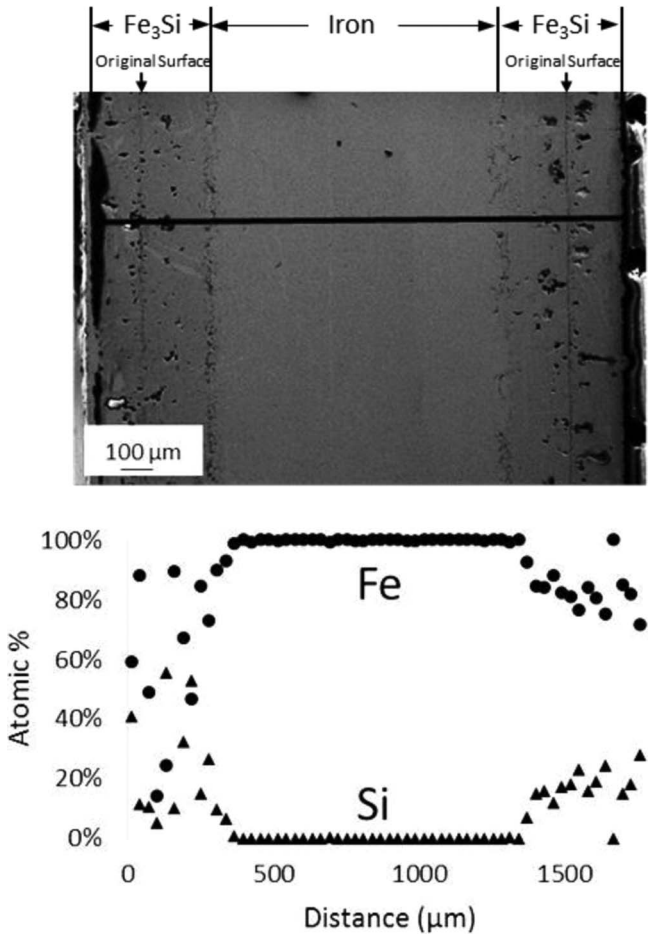


**Figure 5.** Full width cross sectional image of a sample after exposure to a chlorosilane environment for 100 hours at 600°C.

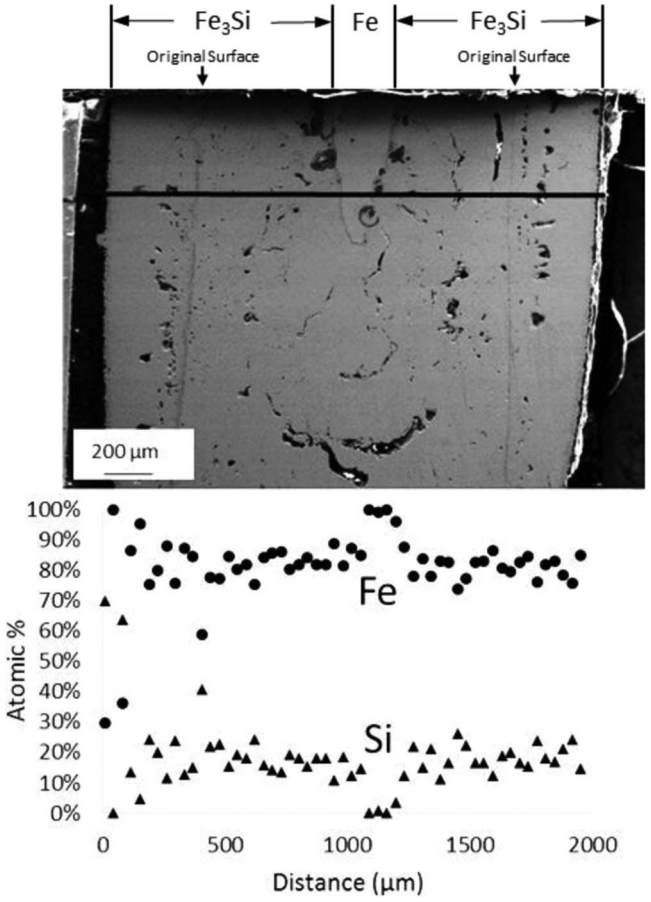


**Figure 6.** Full width cross sectional image of a sample after exposure to a chlorosilane environment for 100 hours at 650°C. The region in the top middle of the image represents remaining, unreacted iron.

of chlorosilane exposure at 550°C. The EDS line scan shows that there is higher silicon content on the surface that tapers to zero in the bulk iron. The total depth of silicon penetration is approximately 6 µm. This agrees with the XRD pattern that indicates both silicon in solution with iron and $Fe_3Si$ in the sample. The full width cross sections and line scans of samples after 100 hours at 600°C and 650°C exposures are shown in Figures 5 and 6 respectively. Because there was gas flow on both sides of the samples, it would be expected that these cross sections and EDS line scans be perfectly symmetrical. When looking at Figures 5 and 6, it appears that the images are symmetrical, but there is some asymmetry in the composition data. This could be due to errors in quantifying EDS, the detection of local non-uniformity, or some slight differences between the tops and bottoms of the sample.

After 600°C exposure (Figure 5), one can see a corrosion layer that has formed on the iron substrate. Looking primarily at the right side of the cross section, it is clear that there is high silicon content at the surface that tapers down to zero in the bulk iron. Based on the atomic concentrations coupled with the XRD patterns, it is clear that the majority of the corrosion scale is $Fe_3Si$. The tapered Si region may represent where silicon has diffused into the iron lattice but is not present in high enough concentrations to form $Fe_3Si$. This trend is also present after exposure at 650°C as displayed in Figure 6. This cross section is interesting because it shows just a small internal region of pure iron remaining. The majority of the sample has been converted to $Fe_3Si$ or iron with silicon in solution. A cross section and line scan taken after exposure for 100 hours at 700°C revealed there was no remaining unreacted iron in the middle of the sample; it had all been converted to an iron silicide. In all samples after exposure at temperatures 600°C and greater, there appears to be two regions of $Fe_3Si$ with the same atomic concentrations. It is proposed that the line separating these two regions marks approximately the location of the original outer edge of the sample. It could be the result of chlorides evaporating from the surface before a silicide could form. $FeCl_2$ and $FeCl_3$ reach a significant vapor pressure at 536°C and 167°C respectively,[5,8] making 600°C a sufficient temperature for reactive evaporation. This reactive evaporation would potentially leave porosity which is visible as a scar or line in the cross sections. There are a few reasons that reactive evaporation may leave a scar. The first is due to some non-uniformity of the reactive evaporation as the chloride and silicide species compete for the iron substrate. This may cause an increase in surface roughness at the initial interface. Also, there may be some residual iron chloride trapped on the surface during corrosion exposure that is washed away during the cross sectioning and polishing procedure. This would also result in increased surface roughness at the original interface and porosity that would be visible in cross sectional FEM analysis. However, these theories were not confirmed in this test.

A high magnification image of the edge of a cross section of a sample after exposure to 100 hours at 700°C is shown in Figure 7. The EDS line scan shows apparent stratification of iron silicide corrosion layers. When corroborated with XRD, there is substantial evidence of FeSi on the surface of the sample with a sharp transition to $Fe_3Si$ behind it. The FeSi region is darker in the micrograph than the $Fe_3Si$ region making it easy to see. It appears to penetrate more in some areas than others rather than being a flat layer. One explanation is that the surface of the sample is rough and full of nodules as shown in Figure 2. The FeSi layer follows the surface of those nodules, making it appear like it is penetrating deeper in some areas than others. Very similar FeSi layers were found on all samples exposed for 100 hours at

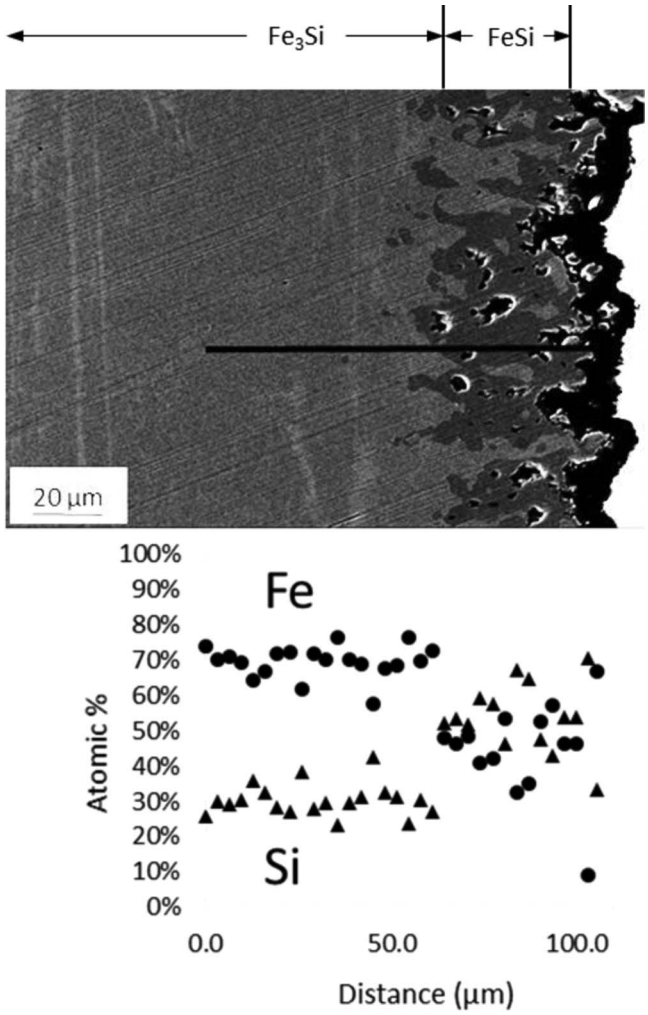


**Figure 7.** High magnification cross sectional image of a sample after exposure to a chlorosilane environment for 100 hours at 700°C. The dark, FeSi on the surface of the sample was seen on all samples exposed at 600°C and higher.

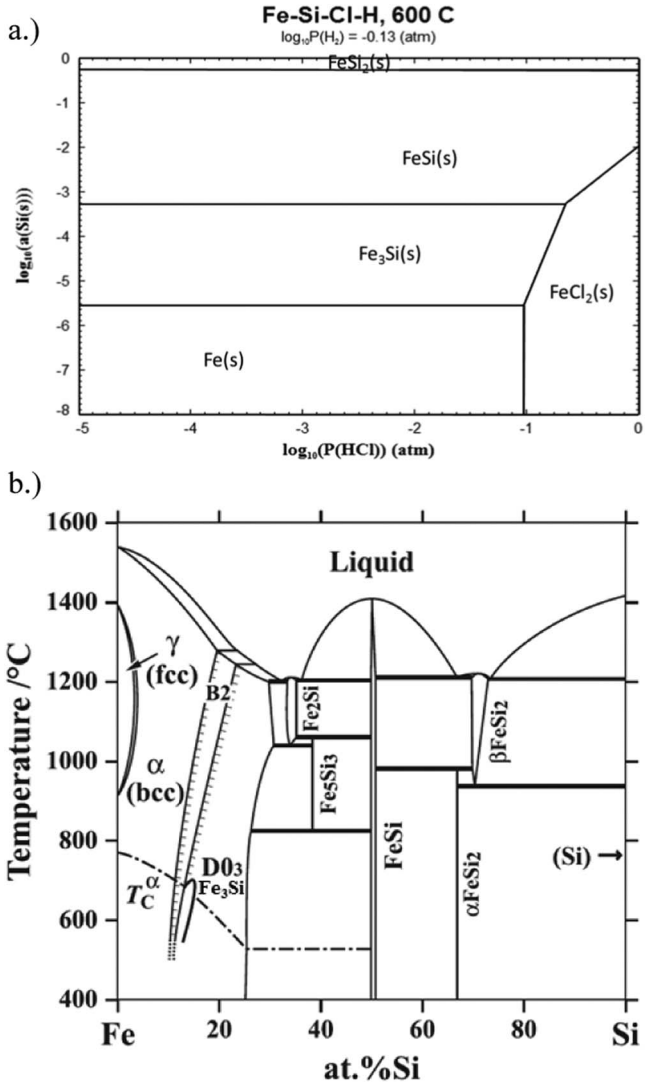


**Figure 8.** Thermodynamic modeling showing a) the predominance diagram for the Iron-Silicon-Chlorine-Hydrogen system at 600°C generated by FactSage and b.) the temperature-composition phase diagram for the iron-silicon system calculated by Kubaschewski[23] and regnerated by Ohnuma.[15] In this diagram, $T_c^{\alpha}$ represents the Currie temperature of the alpha (body centered cubic) phase, B2 represents the Cesium Chloride structure of FeSi, and $D0_3$ represents the cubic structure of $Fe_3Si$.

temperatures greater than or equal to 600°C, with higher temperatures resulting in thicker FeSi layers.

The layers detected by the cross sectional FEM/EDS were predicted by the predominance diagram shown in Figure 8a. This figure displays the HCl activity on the horizontal axis and the silicon activity on the vertical axis with an iron starting material and a constant temperature and $H_2$ partial pressure of 600°C and 0.74 respectively. Diagrams at temperatures from 550–700°C have similar shape with slightly different transition values. This diagram shows that at very low silicon and HCl activity, the iron starting material remains pure iron. This is intuitive and represented by the remaining pure iron in the cross sections of corroded samples. At higher HCl activities and relatively low silicon activity, $FeCl_2$ forms and subsequently vaporizes. At higher Si activity, it takes more HCl to form volatile $FeCl_2$, implying that silicides may impede chloride attack. At increasing Si activity and low HCl activity, the silicide layers get increasingly silicon rich progressing from $Fe_3Si$ to FeSi and $FeSi_2$. This trend was also observed in the analysis with $Fe_3Si$ detected deepest in the bulk and FeSi detected on the surface where the silicon activity is the highest. $FeSi_2$ was not detected in this series of experiments suggesting that the silicon activity was not high enough to form it. Complimentary to the predominance diagram is the iron-silicon phase diagram shown in Figure 8b. This figure shows that silicon is soluble in iron up to approximately 10–12 atomic % between room temperature and 700°C. $Fe_3Si$ exists as a single phase between approximately 12% and 25%, while FeSi is only present as a single phase between 49–51%. In the cross sections analyzed by EDS, there were usually large $Fe_3Si$ layers that had consistent compositions rather than a compositional gradient. Generally this composition was equivalent to stoichiometric $Fe_3Si$. This is comparable to Zhang and Ivey's work with bulk diffusion couples that showed stoichiometric $Fe_3Si$ is favored and forms more quickly than non-stoichiometric $Fe_3Si$.[14] There were some cross sections with areas that had a consistent composition with Si content less than that of stoichiometric $Fe_3Si$. This could be due to a two phase region with the second phase being more iron rich, some unexpected growth of non-stoichiometric $Fe_3Si$, or error in the quantification of EDS.

***Time dependence of corrosion.***—The time dependence of the corrosion scale growth was important to explore to understand how the iron silicides form. This series of experiments was run at 600°C with an input mole fraction of 0.74 $H_2$ and 0.26 STC. These conditions were chosen because they most accurately replicate industrial processes and the temperature dependent study implied that the corrosion layers would form at a reasonable rate. The gravimetric data

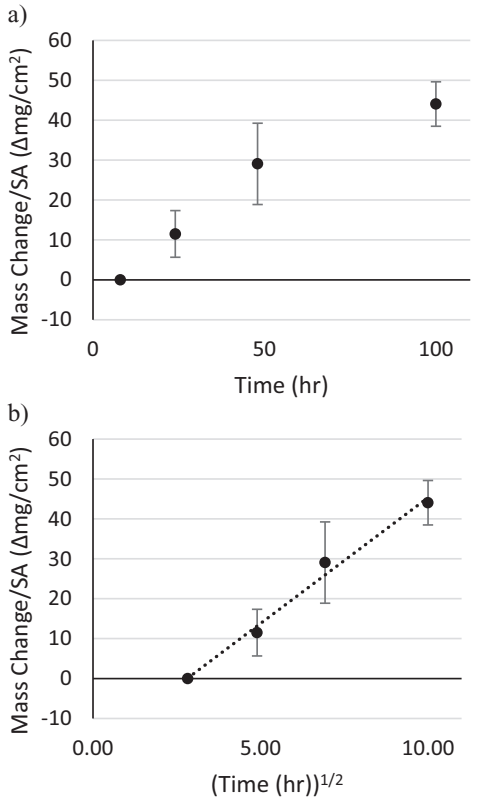


**Figure 9.** The a) specific mass change data and b) transformed gravimetric data for the time dependent study. The transformed data plots mass change vs the square root of time to identify if parabolic kinetics are present. The error bars represent a 95% confidence interval on the mean.

from these exposures is shown in Figure 9a and the plan view micrographs are shown in Figure 10. Figure 9b also includes transformed gravimetric data that shows the mass change per surface area plotted against square root of time. This plot shows how well the corrosion complies with parabolic kinetics. The trend line in this plot shows a relatively good fit with parabolic kinetics with the trend starting at roughly 8 hours rather than 0 hours. This may be due to some initial

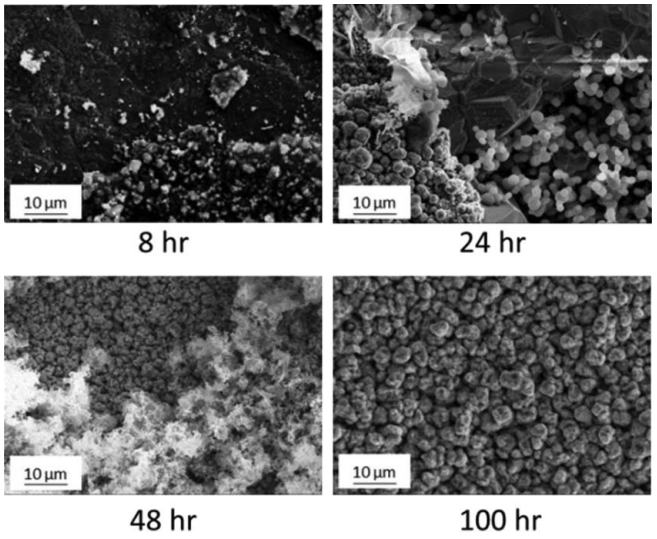


**Figure 10.** The plan view FEM micrographs for the time dependent study. These samples were exposed to a STC/H2 environment for 8, 24, 48, and 100 hours at 600°C.

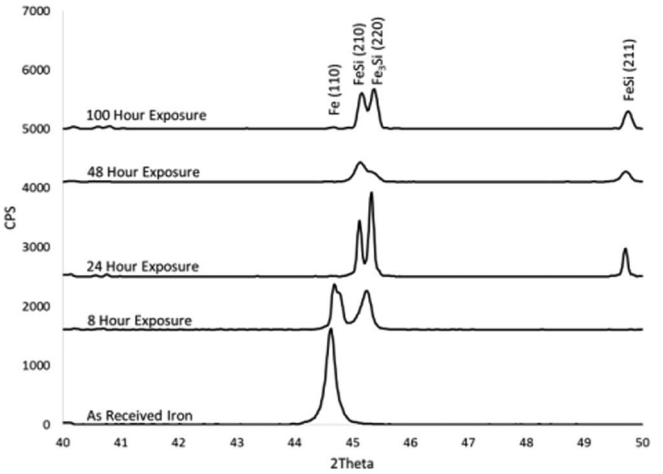


**Figure 11.** The XRD patterns for iron samples after exposure to chlorosilane environments at 600°C for 8, 24, 48, and 100 hours.

chloride formation and vaporization before a silicide layer can form. Diffusion limited, parabolic growth naturally requires a continuous layer for species to diffuse through. The data suggests that this layer establishes itself after 8 hours in these conditions. The plan view FEM and EDS data supports this theory, with primarily iron being detected after 8 hours, and primarily iron and silicon being detected after 24, 48, and 100 hours. Chlorine was not detected in significant quantities on any of the surfaces, as expected from the high vapor pressure of iron chlorides at 600°C.[5,8]

Additional information can be garnered from looking at XRD patterns from these samples. A plot of the patterns is displayed in Figure 11. This plot shows from two theta of 40–50 to capture significant Fe, FeSi, and $Fe_3Si$ peaks.[24–26] A scan of the as received iron is displayed first with a peak corresponding to alpha iron. The scan from the sample after 8 hours of exposure also displays a peak near the location of alpha iron and a peak that corresponds to $Fe_3Si$. The iron peak is shifted slightly to a higher two theta, likely due to silicon substituting into an iron lattice, making the lattice parameters slightly smaller.[27–30] XRD analysis after 24 hours of exposures shows little to no iron on the surface, and primarily detected FeSi and $Fe_3Si$. This trend continued at 48 and 100 hours of exposure. Cross section analysis was used to complement the XRD data. The cross section of the sample after 8 hours of exposure is shown in Figure 12. This shows a large amount of silicon on the surface of the sample that tapers off deeper in the sample. The total depth of silicon penetration is approximately 4 µm. The concentration of silicon is similar to that of stoichiometric $Fe_3Si$ near the surface and less than the solubility limit of silicon in iron (approximately 12 atomic %[23]) deeper in the bulk. This agrees well with the XRD data. A cross section of a sample after 24 hours at 600°C is shown in Figure 13. In this cross section, there is a much larger region similar in composition to $Fe_3Si$ before a similar silicon composition taper to zero atomic %. Again, this agrees with the XRD data that shows primarily $Fe_3Si$ after 24 hours. XRD also indicated FeSi after 24 hours, which was detected with EDS at a higher magnification. Figure 14 shows the cross section and line scan of a sample after exposure at 600°C for 100 hours. This line scan shows stoichiometric FeSi compositions near the surface, a very large region of stoichiometric $Fe_3Si$, and then the silicon concentration tapers to pure iron. The presence of an FeSi layer was confirmed with a higher magnification image and line scan that was similar in character to Figure 7. Similar to the temperature dependent results, these time dependent results can be confirmed by comparing the stratification to the predominance diagram and phase diagram in Figure 8. However, it is important to remember that these diagrams are based solely on thermodynamics and not kinetics. Therefore, they do not predict what layers may form first.

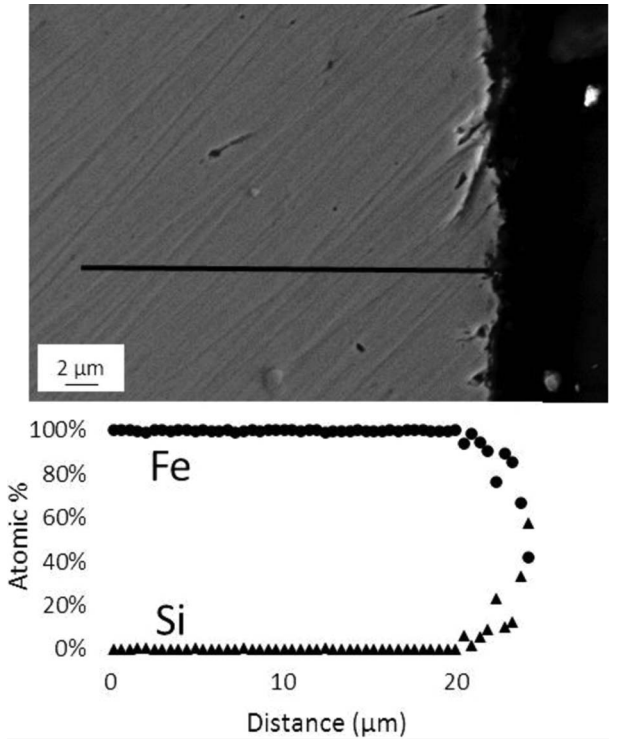


**Figure 12.** High magnification cross sectional image of a sample after exposure to a chlorosilane environment for 8 hours at 600°C.

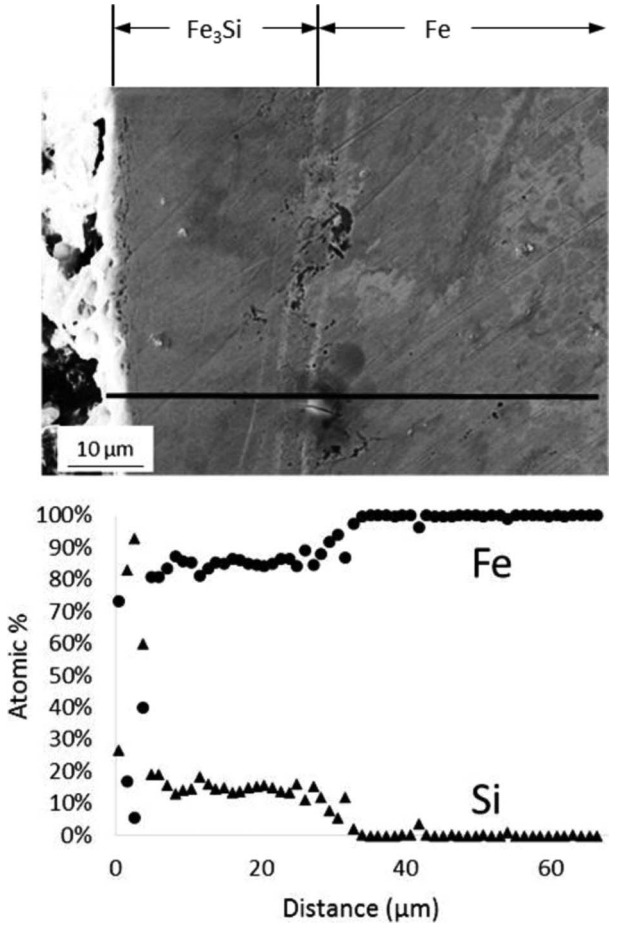


**Figure 13.** High magnification cross sectional image of a sample after exposure to a chlorosilane environment for 24 hours at 600°C.

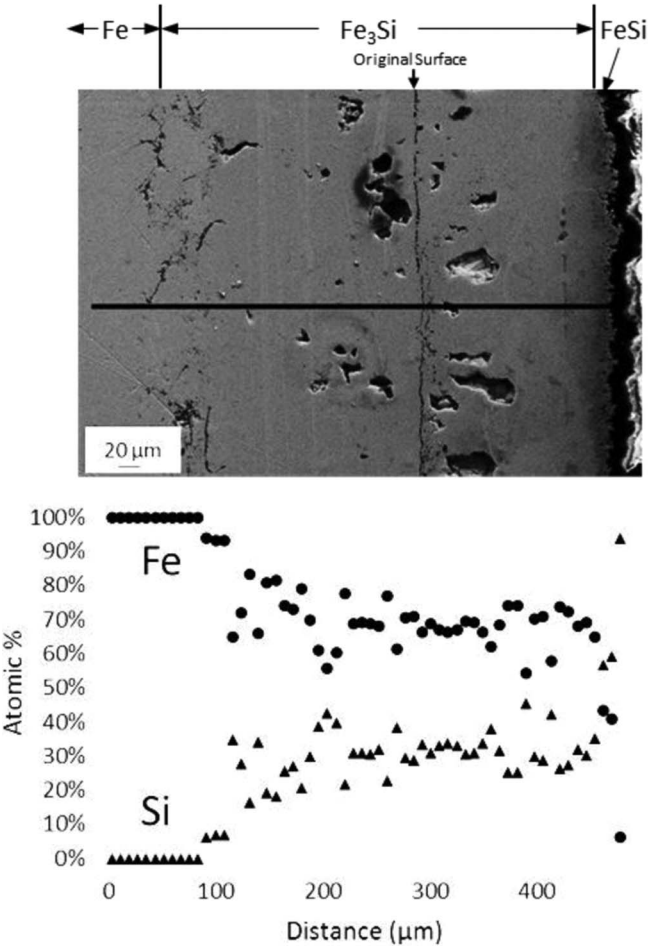


**Figure 14.** High magnification cross sectional image of a sample after exposure to a chlorosilane environment for 100 hours at 600°C.

***Discussion.—***It appears from the temperature dependent study that the corrosion mechanisms are similar for exposure at temperatures greater than or equal to 600°C. Therefore, this discussion will primarily focus on the formation and progression of iron silicide corrosion layers at or above that temperature. A diagram showing the proposed mechanisms of corrosion is displayed in Figure 15. The first step in this process is silicon deposition. In the figure, it is shown as the direct reaction of silicon tetrachloride with hydrogen to form silicon

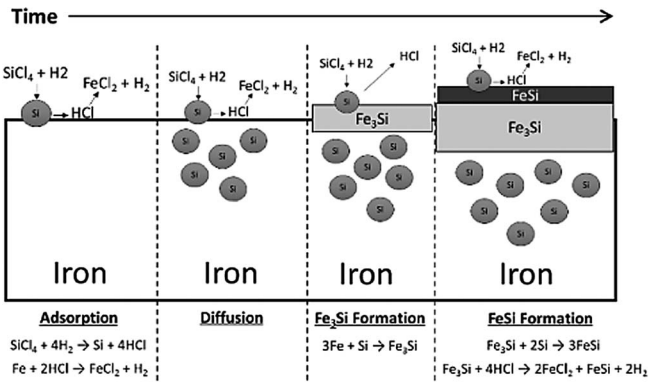


**Figure 15.** Proposed corrosion behavior of iron in chlorosilane environments between 600 and 700°C

and hydrogen chloride. It is likely that there are some intermediate gas phase reactions including the formation of trichlorosilane[1,4] or $SiCl_2$.[12] However, the end result of these gas phase reactions is suggested to be silicon deposition and adsorption onto the iron surface. An alternative to silicon deposition and adsorption is the direct reaction of chlorosilane species with the iron to form iron silicides. This reaction is likely not the dominate mechanism due to the detection of silicon in an iron lattice prior to iron silicide formation.

The hydrogen chloride produced as a result of this silicon deposition very likely reacts with iron forming volatile iron chloride. This is shown in Figure 15 as $FeCl_2$ formation, however $FeCl_3$ is also possible. Once the silicon is deposited on the iron, it starts to diffuse into the iron. Once there is a high enough concentration of silicon on the surface, it reacts with the iron to form $Fe_3Si$. The data after 8 hours of exposure reflects roughly this time period. At this point, there is a thin layer of $Fe_3Si$, some iron saturated with silicon, and a taper of silicon concentration in the iron. The slight mass loss of these samples is also representative of iron chloride formation and evaporation. The next step in the corrosion process involves $Fe_3Si$ growth and FeSi formation. FeSi can form from either the reaction of deposited Si with $Fe_3Si$ or the reaction of $Fe_3Si$ with HCl. These reactions are both displayed in Figure 15. Both cases have been reported in the literature,[13,18] and it is likely that both reactions happen simultaneously. This stage is represented by the data after 24 hours. At this point there is a thin FeSi layer, a large section of $Fe_3Si$, and finally a taper of silicon concentration in the iron. For longer periods of time, it appears that both the $Fe_3Si$ and FeSi continue to grow. At some point, there may be a high enough silicon activity to form $FeSi_2$, but it was not observed in this series of tests.

Previous Mossberg spectroscopy[32] and tracer diffusion investigations[33] have reported that iron diffusion in $Fe_3Si$ is quite fast while silicon diffusion is slow. This indicates that $Fe_3Si$ formation occurs at the $Fe_3Si$-FeSi interface. Additionally, iron diffusion has been reported as the dominate transport mechanism in FeSi.[34] However, iron diffusion is much faster in $Fe_3Si$ than FeSi. This is potentially the reason $Fe_3Si$ scales are much thicker than FeSi scales. An analog to this situation is the layered formation of iron oxides; wüstite, magnetite, and hematite. Wüstite layers are often much thicker than magnetite and hematite layers due to the high iron and oxygen self-diffusion coefficients.[35] Future work could verify this assumption. Additional future work in the field of silicide and chloride formation is to quantify the amount of iron chloride volatilization via precise gravimetric data and corrosion scale thickness and density measurements. If one knew the density and thickness of the silicide scale, the theoretical mass change from silicide formation could be calculated. Deviations from this theoretical mass change could then be related to chloride formation. Then, the establishment of long term paralinear kinetics could be assessed; similar to the work of Maloney and McNallan.[36] However, in this experiment, this calculation could not be done accurately due to bulk silicide layer density variations from a significant amount of porosity, variations in corrosion layer thickness, and significant edge effects due to the relative size of the corrosion scale compared to the original sample.

Figure 15 represents the first time a mechanism of iron corrosion in chlorosilane environments has been proposed. This is significant because understanding how a metal corrodes in a specific environment is the first step in understanding how to protect it from that environment. If any step in the corrosion process can be cut off by alloying or other means, it will prevent the iron from further corrosion and allow for use of low cost iron based alloys in chlorosilane applications. For example, if an alloying element can be added to the iron to reduce the silicon diffusion into the iron lattice, it would impede the formation of $Fe_3Si$ and FeSi, making the corrosion process less detrimental. This may have been the case in the author's previous study on chlorosilane corrosion of AISI 316L.[19] In that study, the 316L corroded approximately $1/8^{th}$ as much as iron in similar conditions as measured by mass change per surface area. This is potentially due to the alloying elements present in 316L such as chromium and nickel impeding silcidation. However, further investigation needs to be done in the field to confirm this assertion.

## Conclusions

In this study, pure iron was exposed to a hydrogen/STC environment at a variety of times (8–100 hours) and temperatures (550–700°C) relevant for understanding the corrosion mechanisms at play. It was discovered that exposures for 100 hours at temperatures between 600 and 700°C resulted in similar mechanisms as indicated by transformed gravimetric data, XRD patterns, and plan view and cross sectional FEM/EDS. These exposures all resulted in thick $Fe_3Si$ layers beneath thinner surface FeSi layers. The higher temperature increased the thickness of these layers to the point where there was no remaining pure iron after the 700°C run. The exposure at 550°C resulted in markedly different corrosion products including a different phase of $Fe_3Si$.

A time dependent study was also conducted at 600°C exposures. In this study, it was discovered that parabolic kinetics exist after an initial scale can be formed. A proposed mechanism for iron silicide formation in chlorosilane environments includes silicon deposition and surface adsorption, silicon diffusion in to the iron lattice, $Fe_3Si$ formation, and FeSi formation. Further understanding of each of these mechanisms and how to prevent them will result in implementation of low cost iron based alloys in chlorosilane service.

## Acknowledgments

We would like to graciously acknowledge GT Advanced Technologies for providing funding and industrial guidance on this project. Additionally, Montana State University College of Engineering provided secondary funding of this project. Finally, we acknowledge Montana State University's Imaging and Chemical Analysis Laboratory (ICAL) for their assistance with surface analysis.

## References

1. W. M. Ingle and M. S. Peffley, *Journal of The Electrochemical Society*, **132**(5), 1236 (1985).
2. T. I. Kamins, *Journal of The Electrochemical Society*, **121**(5), 681 (1974).
3. S. F. Nitodas and S. V. Sotirchos, *Journal of The Electrochemical Society*, **149**(2), C120 (2002).
4. T. O. Sedgwick, *Journal of The Electrochemical Society*, **111**(12), 1381 (1964).
5. P. Daniel and R. Rapp, in *Advances in Corrosion Science and Technology*, M. Fontana and R. Staehle, eds., p. 55–172, Springer US (1976).
6. Y. Ihara, H. Ohgame, K. Sakiyama, and K. Hashimoto, *Corrosion Science*, **21**(12), 805 (1981).
7. N. S. Jacobson, *Oxid Met*, **26**(3–4), 157 (1986).
8. P. Roberge, *Handbook of Corrosion Engineering*, Mcgraw-Hill (1999).
9. J. Y. P. Mui, *Corrosion*, **41**(2), 63 (1985).
10. M. Rebhan, R. Meier, A. Plagge, M. Rohwerder, and M. Stratmann, *Applied Surface Science*, **178**(1–4), 194 (2001).
11. M. Rebhan, M. Rohwerder, and M. Stratmann, *Applied Surface Science*, **140**(1–2), 99 (1999).
12. C. Klam, J. Millet, H. Mazille, and J. Gras, *Journal of Materials Science*, **26**(18), 4945 (1991).
13. N. R. Baldwin and D. G. Ivey, *Journal of Phase Equilibria*, **16**(4), 300 (1995).
14. Y. Zhang and D. G. Ivey, *Journal of Materials Science*, **33**(12), 3131 (1998).
15. I. Ohnuma, S. Abe, S. Shimenouchi, T. Omori, R. Kainuma, and K. Ishida, *ISIJ International*, **52**(4), 540 (2012).
16. J. Acker and K. Bohmhammel, *The Journal of Physical Chemistry B*, **106**(19), 5105 (2002).
17. J. Acker, K. Bohmhammel, G. J. K. van den Berg, J. C. van Miltenburg, and C. Kloc, *The Journal of Chemical Thermodynamics*, **31**(12), 1523 (1999).
18. J. Acker, I. Röver, R. Otto, G. Roewer, and K. Bohmhammel, *Solid State Ionics*, **141–142**, 583 (2001).
19. J. Aller, K. Ellingwood, N. Jacobson, and P. Gannon, *Journal of The Electrochemical Society*, **163**(8), C452 (2016).
20. J. L. Aller, K. Ellingwood, B. Clark, and P. E. Gannon, *ECS Transactions*, **66**(18), 41 (2015).
21. J. L. Aller, P. White, J. Gum, B. Clark, and P. E. Gannon, *ECS Transactions*, **64**(26), 161 (2015).
22. C. W. Bale, P. Chartrand, S. A. Degterov, G. Eriksson, K. Hack, R. Ben Mahfoud, J. Melançon, A. D. Pelton, and S. Petersen, *Calphad*, **26**(2), 189 (2002).
23. O. Kubaschewski, *Iron - Binary Phase Diagrams*, Springer - Verlag, Berlin, Germany (1982).

24. E. A. Owen and E. L. Yates, *The London, Edinburgh, and Dublin Philosophical Magazine and Journal of Science*, **15**(98), 472 (1933).
25. F. A. B. Sidorenko, A. N. Shubina, T. S. Skripova, A. Ye, and L. P. Zelenin, *Physics of Metals and Metallography*, **28**, 91 (1969).
26. J. Waliszewski, L. Dobrzyński, A. Malinowski, D. Satuła, K. Szymański, W. Prandl, T. Brückel, and O. Schärpf, *Journal of Magnetism and Magnetic Materials*, **132**(1), 349 (1994).
27. F. Huyan, R. Larker, P. Rubin, and P. Hedström, *ISIJ International*, **54**(1), 248 (2014).
28. W. C. Leslie, *The physical metallurgy of steels*, Washington: Hempisphere Pub. Corp. New York: McGraw-Hill, Washington: New York (1981).
29. H. Nieswaag and J. W. Nijhof, *MRS Proceedings*, **34**, 411 (1984).
30. M. A. Krishtal, T. A. Sirenko, T. A. É., G. Titenskii, and G. I. Naumov, *Metal Science and Heat Treatment*, **12**(1), 78 (1970).
31. Z. Yu, *Yen K'uang Ts'e Shih*, (3), 231 (1984).
32. B. Sepiol and G. Vogl, *Physical Review Letters*, **71**(5), 731 (1993).
33. A. Gude and H. Mehrer, *Philosophical Magazine A*, **76**(1), 1 (1997).
34. S. Kipp, M. Zöllner, O. Ott, and K. D. Becker, *Solid State Ionics*, **172**(1–4), 407 (2004).
35. W. W. Smeltzer and D. J. Young, *Progress in Solid State Chemistry*, **10**, 17 (1975).
36. M. Maloney and M. McNallan, *Metallurgical Transactions B*, **16**(4), 751 (1985).